

See discussions, stats, and author profiles for this publication at: <https://www.researchgate.net/publication/265851701>

# Computed and Experimental Absorption Spectra of the Perovskite $\text{CH}_3\text{NH}_3\text{PbI}_3$

ARTICLE in JOURNAL OF PHYSICAL CHEMISTRY LETTERS · AUGUST 2014

Impact Factor: 7.46 · DOI: 10.1021/jz501174e

---

CITATIONS

19

---

READS

171

4 AUTHORS, INCLUDING:



Haibin Su

Nanyang Technological University

174 PUBLICATIONS 2,110 CITATIONS

SEE PROFILE



Maria Elisabeth Michel-Beyerle

Nanyang Technological University

188 PUBLICATIONS 6,809 CITATIONS

SEE PROFILE

# Computed and Experimental Absorption Spectra of the Perovskite $\text{CH}_3\text{NH}_3\text{PbI}_3$

Xi Zhu,<sup>†</sup> Haibin Su,<sup>\*,†</sup> Rudolph A. Marcus,<sup>\*,‡,§</sup> and Maria E. Michel-Beyerle<sup>\*,§,||</sup>

<sup>†</sup>Institute of Advanced Studies and School of Materials Science and Engineering, Nanyang Technological University, Singapore 639798

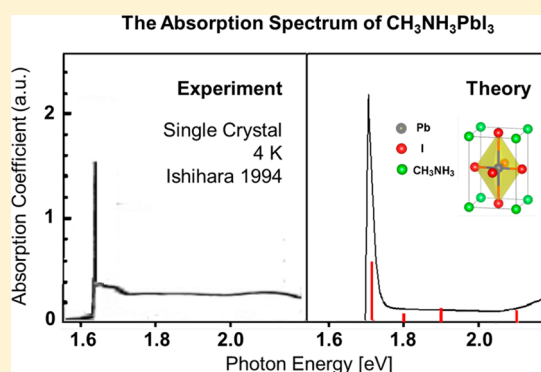
<sup>‡</sup>Noyes Laboratory, California Institute of Technology, Pasadena California 91125, United States

<sup>§</sup>School of Physical and Mathematical Sciences, Singapore 637371

<sup>||</sup>TUM CREATE, Singapore 138602

**ABSTRACT:** Electronic structure and light absorption properties of the perovskite  $\text{CH}_3\text{NH}_3\text{PbI}_3$  are investigated by relativistic density functional theory with quasiparticle GW corrections and many-body interactions. The nature of the Wannier exciton is studied by solving the Bethe–Salpeter equation augmented with the analysis of a conceptual hydrogen-like model. The computed absorption spectrum unravels a remarkable absorption “gap” between the first two absorption peaks. This discontinuity is maintained in the calculated tetragonal structure that, however, is not stable at low temperature. Most importantly, the discontinuity is also observed in the experimental absorption spectrum of the orthorhombic single crystal at low temperature (4 K). However, in contrast to the single crystal, in a polycrystalline perovskite film at 5 K the “gap” is filled by a monotonously increasing absorption throughout the visible range. This feature of thin films points to the potential significance of defect absorption for the excellent light harvesting properties of perovskite-based solar cells.

**SECTION:** Molecular Structure, Quantum Chemistry, and General Theory



Perovskites of the organo-lead halide type, initially used as a dye replacement to act as light absorber,<sup>1</sup> have recently emerged as a promising component of solar cells due to their high efficiency of solar-to-electrical power conversion. This efficiency, reaching beyond 15%, is equally high when using mesoporous semiconductor supports for the photoactive perovskite layer<sup>2–5</sup> as well as a planar perovskite layer between electrodes.<sup>6–9</sup> The perovskite mostly employed in these successful solar devices is methylammonium lead iodide ( $\text{CH}_3\text{NH}_3\text{PbI}_3$ ) that has been shown to act all-in-one as light absorber, photon-charge converter, and charge transporter.<sup>10–14</sup>

The primary steps of light absorption, charge separation/recombination, and electron/hole transport have been studied in femtosecond time resolution using polycrystalline perovskite films on mesoporous metal oxide substrates (e.g., titania and alumina) as well as on flat quartz supports.<sup>15,16</sup> Such films were usually excited in the range between 400 to 600 nm at energies that are exceeding the lowest exciton transition by more than 0.5 eV. For these experiments  $\text{CH}_3\text{NH}_3\text{PbI}_3$  was deposited on the surfaces by spin coating of a colloidal solution that contained both components, lead iodide, and ammonium iodide. Upon evaporation of the solvent a polycrystalline layer was formed and thermally annealed. The crystalline character of the so-formed perovskite layers was confirmed by X-ray diffraction.<sup>17,18</sup> The average thickness of such films was in the

range of 200–500 nm as determined by scanning electron microscopy.

The emphasis of this paper is on the absorption spectrum of the  $\text{CH}_3\text{NH}_3\text{PbI}_3$  perovskite, which has proven itself to be a perfect solar light harvester. This feature and the urgent need for optimization of this type of low-fabrication-cost solid-state solar cell prompted us to perform ab initio quantum chemical calculations of the electronic states involved. As a first step, we calculated the long wavelength absorption spectrum and compared it with the experimental, low temperature (4 K) spectrum by Ishihara<sup>19</sup> taken for a single crystal.

In the present study, we focus on both the orthorhombic phase, as this phase is the stable one at low temperature, and the tetragonal structure, which is operative in the room temperature range of solar cells. The 3-dimensional crystal structure of the tetragonal  $\text{CH}_3\text{NH}_3\text{PbI}_3$  perovskite<sup>17</sup> depicted in Figure 1 exhibits a slight distortion and tilting of the  $\text{PbI}_6$  octahedra with respect to the *c* axis and shows the disorder of the methylammonium (MA) cations. The numerically optimized lattice parameters presented in the caption of Figure 1

**Received:** June 9, 2014

**Accepted:** August 22, 2014

**Published:** August 22, 2014



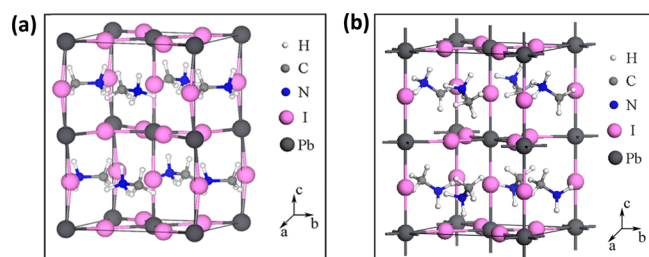


**Figure 1.** The  $\text{CH}_3\text{NH}_3\text{PbI}_3$  crystal structures. (a) The orthorhombic phase (space group  $Pna2_1$ ) with the optimized lattice parameters (experimental values<sup>17</sup> in parentheses):  $a = 8.87$  (8.86) Å,  $b = 8.60$  (8.58) Å,  $c = 12.70$  (12.62) Å. (b) The tetragonal phase (space group  $I4/mcm$ ) with the optimized lattice parameters:  $a = b = 8.86$  (8.86) Å,  $c = 12.70$  (12.66) Å.

are in good agreement with the experimental values<sup>17</sup> and with values also used in previous DFT calculations discussed below. **Lowest Exciton Transition.** Before going into the details of the present calculations, we comment on previous theoretical treatments. DFT-based band structure calculations<sup>20–22</sup> were able to reproduce the experimental absorption edge in the 1.6 eV region,<sup>19,23</sup> even though they did not account for the strong spin–orbit coupling (SOC) of the heavy metal. When SOC was included, the DFT-calculated energy gap for the tetragonal high-temperature phase turned out to be less than the experimental value by more than 1 eV.<sup>24–26</sup> In this paper, we have now taken a significant step to correct the self-energy error inherent in DFT calculations. Upon adjusting the DFT method to GW,<sup>27</sup> we obtain 1.69 and 1.57 eV for the lowest band–band transition in the orthorhombic and tetragonal perovskite structure, respectively. [While this paper was in the stage of submission, DFT-GW calculations were published that agree with the band gap computed in the present paper.<sup>39</sup>] The GW approach developed to perform the quasiparticle corrections to the DFT energies aims at an improved description of the simplest charged excitation, that is, the addition or removal of an electron. It was successful in the computation of photoelectron spectra that agree well with experimental measurements.<sup>28</sup> Moreover, the electron–hole interaction had to be included in computing optical absorption spectra, which prompted us to solve the Bethe–Salpeter equation (BSE) in the basis set of quasi-electron and quasi-hole states.<sup>29</sup>

**Absorption Spectrum.** First, we computed the absorption spectrum of the orthorhombic phase, which is the stable structure at temperatures below 162 K<sup>19</sup> and for which the experimental absorption spectrum of the single crystal at 4 K is available.<sup>19,23</sup> Details are given in the section Computational Methodology. In the orthorhombic structure, the lowest exciton transition is computed to be at 1.69 eV (Figure 2b). This value is in perfect agreement with the narrow absorption feature at 1.64 eV shown in Figure 2a. The computed spectrum also reveals that the broadening of the next higher, second absorption band—also seen in the experimental spectrum Figure 2a—is caused by an accumulation of numerous higher transitions. In Figure 2b, the computed maximum at higher energy underestimates the experimental maximum, which appears at 2.77 eV.<sup>19</sup> This discrepancy is not surprising in view of the limited size of active space chosen in these calculations. In addition, it is interesting to observe that in the inherently disordered tetragonal structure shown in Figure 1, this second, high energy transition is more red-shifted as

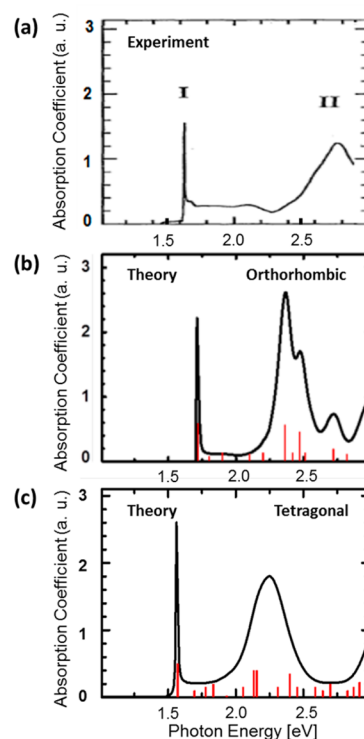


**Figure 2.** Experimental and computed absorption spectra of  $\text{CH}_3\text{NH}_3\text{PbI}_3$ . (a) Experimental absorption spectrum of the single crystal at 4 K<sup>19</sup> in its orthorhombic structure. (b) Absorption spectrum based on the present band structure calculations for the orthorhombic phase. (c) Absorption spectrum based on the present band structure calculations for the tetragonal phase.

compared to the ordered structures of the orthorhombic phase. Nevertheless, the fingerprint of the low temperature spectra of both structures is a wide gap between the lowest exciton transition and the bundled transitions contributing to the next higher band. In contrast, the variation of the computed energy of the lowest exciton transition at 1.53 and 1.69 eV for the tetragonal and orthorhombic phases, respectively, nicely captures the experimental observations.<sup>19</sup>

**Exciton Binding Energy.** To investigate the binding strength of the exciton state in the tetragonal room temperature phase relevant for solar cells, we calculated the binding energy of the lowest exciton. The notion of a weakly bound exciton with a binding energy of the order of the thermal energy  $k_B T$  at room temperature is corroborated within the framework of (i) the semiclassical model of a Wannier exciton and (ii) the present quantum-chemical calculations. (i) To gain better understanding of the weak Coulomb coupling of the Wannier exciton, a hydrogen-like model is constructed as follows: If  $p_\phi$  denotes the orbital angular momentum of the exciton, then the binding energy  $E$  of the exciton is  $E = (-e^2/\epsilon r) + (p_\phi^2/2\mu r^2)$ , where  $e$  denotes the elementary electronic charge,  $\epsilon$  is the dielectric constant for the relevant exciton frequency,  $r$  is the electron–hole distance in the bound exciton state, and  $\mu$  is the reduced mass of exciton. To obtain the exciton radius  $r$ , we set  $\partial E/\partial r = 0$  and obtain  $r = \epsilon p_\phi^2/\mu e^2$ . Hence,  $E = (-e^2/\epsilon r) + (e^2/2\epsilon r) = (-e^2/2\epsilon r)$ . Therefore, if one knows the exciton radius  $r$ , then one knows  $E$ , without having to know the reduced mass of the exciton. Of course, the radius originates from magnetic experiments that also determine the effective mass. For this lead-halide-based perovskite, the high-frequency dielectric

constant is 6.5<sup>30</sup> and exciton's radius is deduced to be 28 Å using the measured diamagnetic coefficient in the magneto-absorption spectra.<sup>30</sup> One subsequently obtains the binding energy to be 50 meV. (ii) We define the exciton binding energy  $E_b$  as the difference between the GW band gap and the optical absorption energy computed by solving Bethe–Salpeter equation. Details are given in the section Computational Methodology. So,  $E_b = E_{\text{GW}} - E_{\text{absorption}}$ . The computed the binding energy is 40 meV. This lowest lying exciton is of Wannier-type with charge transfer character. As a result, the exciton binding energies computed within both the hydrogen-like model and ab initio are in nice agreement. On the basis of this small binding energy, the low temperature excitonic transition of the tetragonal perovskite phase would be located at 1.53 eV. Such a value would coincide with the room temperature absorption edge<sup>1,2,10</sup> and the weak electronic coupling of the low energy exciton state supports the view that at room temperature, the lowest exciton is de facto degenerate with the band states.

**Band Structure.** For the tetragonal-disordered phase most relevant for solar cells the details of the band structure calculations are given in the energy scheme of Figure 3. The

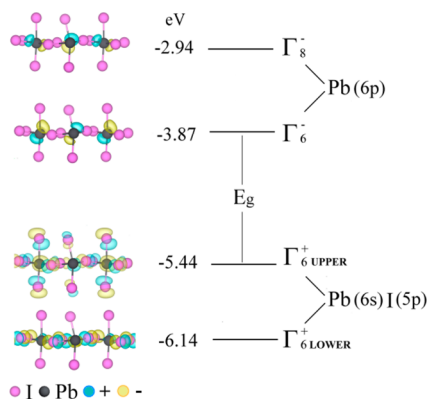


**Figure 3.** Contour plots of wave functions of  $\text{CH}_3\text{NH}_3\text{PbI}_3$  in its tetragonal phase and the respective energy levels. For the sake of clarity, the methylammonium cations are not shown.

edge of the valence band  $\Gamma_{6\text{UPPER}}^+$  is set to be  $-5.43$  eV below vacuum, as measured by ultraviolet photoelectron spectroscopy.<sup>2</sup> Both  $\Gamma_6^-$  and  $\Gamma_8^-$  states consist predominantly of (Pb 6p) orbitals. The out-of-phase coupling between (Pb 6s) and (I 5p) orbitals as shown in the wave functions illustrates the antibonding character of  $\Gamma_{6\text{UPPER}}^+$  and  $\Gamma_{6\text{LOWER}}^+$ . The state  $\Gamma_{6\text{UPPER}}^+$  is composed of 5p orbitals from both out of plane and in plane iodides, whereas  $\Gamma_{6\text{LOWER}}^+$  only involves 5p orbitals from equatorial ones. The antibonding interaction between the Pb (6s) and I (5p) orbitals leads to the strong dispersive character along the  $\Gamma \rightarrow \text{X}$  and  $\Gamma \rightarrow \text{R}$  directions. The relative weak dispersion observed along  $\text{X} \rightarrow \text{R}$  is due to the anisotropic feature in the  $a$ – $b$  plane. Similarly, the strong coupling among (Pb 6p) orbitals across the corner-bound iodide results in the appreciably dispersive conduction bands, as shown in the band structure of Figure 4. There, the states  $\Gamma_{6\text{UPPER}}^+$  and  $\Gamma_{6\text{LOWER}}^+$  are denoted by VB1 and VB2, the states  $\Gamma_6^-$  and  $\Gamma_8^-$  by CB1 and CB2, respectively. In the Poglitsch–Weber crystal structure,<sup>17</sup> the orientation of the C–N axis in the MA cations has rotational freedom that leads to a high degree of disorder. In the conceptually simplest model, we can expect that the density of states associated with the octahedral iodides is predom-

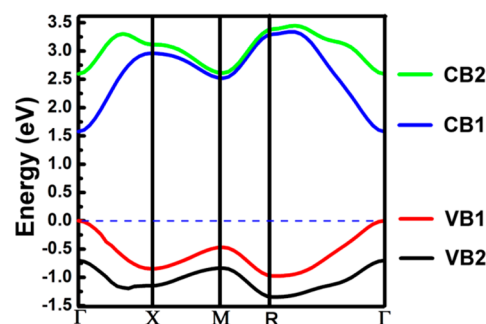


**Figure 4.** Band structure of  $\text{CH}_3\text{NH}_3\text{PbI}_3$  in its tetragonal phase computed by GW-augmented DFT method. The energy of the valence band maximum is set to be zero.

inantly affected because disordered MA cations are in direct electrostatic interaction with these anions and it is this interaction that stabilizes the  $\text{PbI}_6$  octahedra in the lattice of this perovskite. As a consequence, distortions of these octahedra and an unbalanced ratio of organic cations and iodides may affect the absorption spectrum.

**Conclusions.** In contrast to the absorption spectrum of the single perovskite crystal in Figure 2a, the spectrum of a polycrystalline film<sup>23</sup> shows a continuous featureless increase from the absorption edge to the 400 nm region. This monotonously increasing absorption is clearly not covered by the band structure of the perfect single crystal valid at zero temperature. Instead, the computed spectrum (Figure 2b) as well as its experimental counterpart (Figure 2a) is characterized by a sharp exciton transition forming the absorption edge and a broad band at higher energy, the two features being separated by an unstructured absorption “gap” in which many transitions with weak oscillatory strength are subsumed.

In the low temperature (0 K) calculation, the exciton peak is indistinguishable on the energy scale in Figure 2 from the band edge energy as there is no absorption below the peak and a finite absorption at energies above the band edge. Instead, for a semiconductor with disorder, there would be an Urbach/Lifshitz tail,<sup>31</sup> resulting from the disorder stripping band states near the band edge and placing them into the adjacent band gap, thereby removing the discontinuity in the absorption spectrum of the ordered crystalline system. This effect may serve as an experimental criterion for the disordered state of the solid as encountered in thin perovskite films and may be instrumental for the excellent light harvesting properties of the perovskite-based solar cells. Apart from the abundance of surface states in polycrystalline films, in the case of this MA lead iodide, the disorder may be due to a large variety of point defects including vacancies of all three ions causing the enormous sensitivity of the solar device performance to the preparation conditions.

## ■ COMPUTATIONAL METHODOLOGY

First-principles electronic structure calculations have been performed by the density functional theory method (DFT), with the PBE type of the generalized gradient approximation to describe the exchange–correlation functional.<sup>32</sup> Fully relativistic norm-conserving pseudopotentials are applied for the spin–orbit coupling (SOC) calculations.<sup>33</sup> We use 70 Ry kinetic energy cutoff for the wave function until forces acting on each atom are less than 0.01 eV/Å. A  $4 \times 4 \times 2$  K sampling grid is used for integration. Beyond the DFT–PBE level, we



also apply the quasiparticle corrections to the PBE eigenvalues, by using a screened Coulomb potential and the Green's function for the self-energy operator according to the GW approximation. The plasmon-hole approximation<sup>34</sup> is applied for treating the screening by solving the Bethe–Salpeter equation<sup>35</sup>

$$(E_{c\bar{k}} - E_{v\bar{k}})A_{cv\bar{k}}^s + \sum_{c',v',\bar{k}'} \langle v\bar{k}|K^{eh}|c'\bar{k}' \rangle A_{c'v'\bar{k}'}^s = \Omega^s A_{cv\bar{k}}^s \quad (1)$$

where  $A_{cv\bar{k}}^s$  is the exciton wave function,  $K^{eh}$  is the electron hole coupling kernel including the exchange interaction and attractive, screened direct Coulomb interaction,  $\Omega^s$  is the exciton energy, and  $E_{c\bar{k}}$  and  $E_{v\bar{k}}$  are the quasiparticle energies of the electron and hole states, respectively. The imaginary part of dielectric function is calculated within the linear response theory as<sup>36,37</sup>

$$\varepsilon_2(\omega) = \frac{4\pi}{\omega^2} \sum_{c,v,\bar{k}} \delta(\omega - \Omega^s) |A_{cv\bar{k}}^s \langle \bar{k}c|\hat{p} \cdot \hat{e}|\bar{k}v \rangle|^2 \quad (2)$$

where  $\hat{p}$  is the momentum operator,  $\hat{e}$  is the polarization vector,  $|\bar{k}c \rangle$  ( $|\bar{k}v \rangle$ ) is the wave function of electron (hole) state. The real part of the dielectric function,  $\varepsilon_1(\omega)$ , can be generated from  $\varepsilon_2(\omega)$  with the Kramers–Kronig relation<sup>38</sup>

$$\varepsilon_1(\omega) = 1 + \frac{2}{\pi} P \int_0^\infty \frac{\varepsilon_2(\omega') \omega' d\omega'}{\omega'^2 - \omega^2} \quad (3)$$

where  $P$  denotes the principle value. Then, the light absorption coefficient,  $\alpha$ , can be computed by

$$\alpha = 2\omega \left[ \frac{(\varepsilon_1^2(\omega) + \varepsilon_2^2(\omega))^{1/2} - \varepsilon_1(\omega)}{2} \right]^{1/2} \quad (4)$$

following ref 38.

## AUTHOR INFORMATION

### Corresponding Authors

\*H. Su. E-mail: hbsu@ntu.edu.sg.

\*R. A. Marcus. E-mail: ram@caltech.edu.

\*M. E. Michel-Beyerle. E-mail: mariaelisabeth@ntu.edu.sg.

### Notes

The authors declare no competing financial interest.

## ACKNOWLEDGMENTS

We are deeply indebted to Professor Teruya Ishihara for helpful comments on perovskite optical properties and for the agreement to use his absorption spectrum. H.B.S. gratefully acknowledges the access to the High Performance Computing Center at NTU. R.A.M. thanks the ONR and ARO for their support. M.E.M.B. is grateful to the Nanyang Technical University for supporting the Biophysics Center.

## REFERENCES

- (1) Kojima, A.; Teshima, K.; Shirai, Y.; Miyasaka, T. Organometal Halide Perovskites as Visible-Light Sensitizers for Photovoltaic Cells. *J. Am. Chem. Soc.* **2009**, *131*, 6050–6051.
- (2) Kim, H.-S.; Lee, C.-R.; Im, J.-H.; Lee, K.-B.; Moehl, T.; Marchioro, A.; Moon, S.-J.; Humphry-Baker, R.; Yum, J.-H.; Moser, J. E.; et al. Lead Iodide Perovskite Sensitized All-Solid-State Submicron Thin Film Mesoscopic Solar Cell with Efficiency Exceeding 9%. *Sci. Rep.* **2012**, *2*, 591.
- (3) Burschka, J.; Pellet, N.; Moon, S.-J.; Humphry-Baker, R.; Gao, P.; Nazeeruddin, M. K.; Grätzel, M. Sequential Deposition as a Route to High-Performance Perovskite-Sensitized Solar Cells. *Nature* **2013**, *499*, 316–319.
- (4) Etgar, L.; Gao, P.; Xue, Z.; Peng, Q.; Chandiran, A. K.; Liu, B. Mesoscopic  $\text{CH}_3\text{NH}_3\text{PbI}_3/\text{TiO}_2$  Heterojunction Solar Cells. *J. Am. Chem. Soc.* **2012**, *134*, 17396–17399.
- (5) Grätzel, C.; Zakeeruddin, S. M. Recent Trends in Mesoscopic Solar Cells Based on Molecular and Nanopigment Light Harvesters. *Mater. Today* **2013**, *16*, 11–18.
- (6) Liu, M.; Johnston, M. B.; Snaith, H. J. Efficient Planar Heterojunction Perovskite Solar Cells by Vapour Deposition. *Nature* **2013**, *501*, 395–398.
- (7) Ball, J. M.; Lee, M. M.; Hey, A.; Snaith, H. J. Low-Temperature Processed Meso-Superstructured to Thin-Film Perovskite Solar Cells. *Energy Environ. Sci.* **2013**, *6*, 1739–1743.
- (8) Abrusci, A.; Stranks, S. D.; Docampo, P.; Yip, H.-L.; Jen, A. K.-Y.; Snaith, H. J. High Performance Perovskite-Polymer Hybrid Solar Cells via Electronic Coupling with Fullerene Monolayers. *Nano Lett.* **2013**, *13*, 3124–3128.
- (9) Eperon, G. E.; Burlakov, V. M.; Docampo, P.; Goriely, A.; Snaith, H. J. Morphological Control for High Performance, Solution-Processed Planar Heterojunction Perovskite Solar Cells. *Adv. Funct. Mater.* **2013**, *24*, 151–157.
- (10) Kim, H.-S.; Lee, J.-W.; Yantara, N.; Boix, P. P.; Kulkarni, S. A.; Mhaisalkar, S. G.; Grätzel, M.; Park, N.-G. High Efficiency Solid-State Sensitized Solar Cell-Based on Submicrometer Rutile  $\text{TiO}_2$  Nanorod and  $\text{CH}_3\text{NH}_3\text{PbI}_3$  Perovskite Sensitizer. *Nano Lett.* **2013**, *13*, 2412–2417.
- (11) Noh, J. H.; Im, S. H.; Heo, J. H.; Mandal, T. N.; Seok, S. I. Chemical Management for Colorful, Efficient, and Stable Inorganic–Organic Hybrid Nanostructured Solar Cells. *Nano Lett.* **2013**, *13*, 1764–1769.
- (12) Bi, D.; Yang, L.; Boschloo, G.; Hagfeldt, A.; Johansson, E. M. J. Effect of Different Hole Transport Materials on Recombination in  $\text{CH}_3\text{NH}_3\text{PbI}_3$  Perovskite-Sensitized Mesoscopic Solar Cells. *J. Phys. Chem. Lett.* **2013**, *4*, 1532–1536.
- (13) Im, J.-H.; Lee, C.-R.; Lee, J.-W.; Park, S.-W.; Park, N.-G. 6.5% Efficient Perovskite Quantum-Dot-Sensitized Solar Cell. *Nanoscale* **2011**, *3*, 4088–4093.
- (14) Kim, H.-S.; Mora-Sero, I.; Gonzalez-Pedro, V.; Fabregat-Santiago, F.; Juarez-Perez, E. J.; Park, N.-G.; Bisquert, J. Mechanism of Carrier Accumulation in Perovskite Thin-Absorber Solar Cells. *Nat. Commun.* **2013**, *4*, 2242.
- (15) Xing, G.; Mathews, N.; Sun, S.; Lim, S. S.; Lam, Y. M.; Grätzel, M.; Mhaisalkar, S. G.; Sum, T. C. Long-Range Balanced Electron- and Hole-Transport Lengths in Organic–Inorganic  $\text{CH}_3\text{NH}_3\text{PbI}_3$ . *Science* **2013**, *342*, 344–347.
- (16) Stranks, S. D.; Eperon, G. E.; Grancini, G.; Menelaou, C.; Alcocer, M. J. P.; Leijtens, T.; Herz, L. M.; Petrozza, A.; Snaith, H. J. Electron-Hole Diffusion Lengths Exceeding 1 Micrometer in an Organometal Trihalide Perovskite Absorber. *Science* **2013**, *342*, 341–344.
- (17) Poglitsch, A.; Walter, D. Dynamic Disorder in Methylammoniumtrihalogenplumbates Observed by Millimeter Wave Spectroscopy. *J. Chem. Phys.* **1987**, *87*, 6373–6378.
- (18) Baikie, T.; Fang, Y.; Kadro, J. M.; Schreyer, M. K.; Wei, F.; Mhaisalkar, S. G.; Grätzel, M.; White, T. Synthesis and Crystal Chemistry of the Hybrid Perovskite  $(\text{CH}_3\text{NH}_3)\text{PbI}_3$  for Solid State Sensitized Solar Cell Applications. *J. Mater. Chem. A* **2013**, *1*, 5628–5641.
- (19) Ishihara, T. Optical Properties of PbI<sub>2</sub>-Based Perovskite Structures. *J. Lumin.* **1994**, *61*, 269–274.
- (20) Umebayashi, T.; Asai, K.; Kondo, T.; Nakao, A. Electronic Structures of Lead Iodide Based Low-Dimensional Crystals. *Phys. Rev. B* **2003**, *155405*–(1–6).
- (21) Mosconi, E.; Amat, A.; Nazeeruddin, K.; Grätzel, M.; Angelis, F. First-Principles Modeling of Mixed Halide Organometal Perovskites

for Photovoltaic Applications. *J. Phys. Chem. C* **2013**, *117*, 13902–13913.

(22) Wang, Y.; Gould, T.; Dobson, J. F.; Zhang, H.; Yang, H.; Yao, X.; Zhao, H. Density Functional Theory Analysis of Structural and Electronic Properties of Orthorhombic Perovskite  $\text{CH}_3\text{NH}_3\text{PbI}_3$ . *Phys. Chem. Chem. Phys.* **2014**, *4*, 1424–1429.

(23) Tanaka, K.; Takahashi, T.; Ban, T.; Kondo, T.; Uchida, K.; Miura, N. Comparative Study on the Excitons in Lead-Halide-Based Perovskite-Type Crystals  $\text{CH}_3\text{NH}_3\text{PbBr}_3$  and  $\text{CH}_3\text{NH}_3\text{PbI}_3$ . *Solid State Commun.* **2003**, *127*, 619–623.

(24) Even, J.; Pedesseau, L.; Jancu, J.; Katan, C. Importance of Spin–Orbit Coupling in Hybrid Organic/Inorganic Perovskites for Photovoltaic Applications. *J. Phys. Chem. C* **2013**, *4*, 2999–3005.

(25) Even, J.; Pedesseau, L.; Jancu, J.; Katan, C. DFT and  $k \cdot p$  Modelling of the Phase Transitions of Lead and Tin Halide Perovskites for Photovoltaic Cells. *Phys. Status Solidi RRL* **2014**, *8*, 31–35.

(26) Giorgi, G.; Fujisawa, J.-I.; Segawa, H.; Yamashita, K. Small Photocurrent Effective Masses Featuring Ambipolar Transport in Methylammonium Lead Iodide Perovskite: A Density Functional Analysis. *J. Phys. Chem. Lett.* **2013**, *4*, 4213–4215.

(27) Hedin, L. New Method for Calculating the One-Particle Green's Function with Application to the Electron-Gas Problem. *Phys. Rev.* **1965**, *139*, A796–A823.

(28) Onida, G.; Reining, L. R. A. Electronic Excitations: Density-Functional versus Many-Body Green's-Function Approaches. *Rev. Mod. Phys.* **2002**, *74*, 601–659.

(29) Robertson, J. High Dielectric Constant Oxides. *Eur. Phys. J.: Appl. Phys.* **2004**, *28*, 265–291.

(30) Hirasawa, M.; Ishihara, T.; Goto, T.; Uchida, K.; Miura, N. Magnetoabsorption of the Lowest Exciton in Perovskite. *Physica* **1994**, *201*, 427–430.

(31) Boer, K. W. *Survey of Semiconductor Physics, Electrons and Other Particles in Bulk Semiconductors*; van Nostrand Reinhold: New York, 1990.

(32) Perdew, J.; Burke, K.; Ernzerhof, M. Generalized Gradient Approximation Made Simple. *Phys. Rev. Lett.* **1996**, *77*, 3865–3868.

(33) Giannozzi, P.; Baroni, S.; Bonini, N.; Calandra, M.; Car, R.; Cavazzoni, C.; Ceresoli, D.; Chiarotti, G. L.; Cococcioni, M.; Dabo, I.; et al. QUANTUM ESPRESSO: A Modular and Open-Source Software Project for Quantum Simulations of Materials. *J. Phys.: Condens. Matter* **2009**, *21*, 395502.

(34) Godby, R. W.; Needs, P. J. Metal-Insulator Transition in Kohn-Sham Theory and Quasiparticle Theory. *Phys. Rev. Lett.* **1989**, *62*, 1169–1172.

(35) Marini, A.; Hogan, C.; Gruning, M.; Varsano, D. Y. An Ab Initio Tool for Excited State Calculations. *Comput. Phys. Commun.* **2009**, *180*, 1392–1403.

(36) Rohlfing, M.; Louie, S. G. Electron-Hole Excitations and Optical Spectra from First Principles. *Phys. Rev. B* **2000**, *62*, 4927–4944.

(37) Chang, E. K.; Rohlfing, M.; Louie, S. G. Excitations and Optical Properties of  $\alpha$ -Quartz. *Phys. Rev. Lett.* **2000**, *85*, 2613–2616.

(38) Wooten, F. *Optical Properties of Solids*; Academic Press: New York, 1972.

(39) Amat, J.; Mosconi, E.; Ronca, E.; Quarti, C.; Umari, P.; Nazeeruddin, M. K.; Grätzel, M.; De Angelis, F. Cation-Induced Band-Gap Tuning in Organohalide Perovskites: Interplay of Spin–Orbit Coupling and Octahedra Tilting. *Nano Lett.* **2014**, DOI: 10.1021/nl5012992.